CAMBRIDGE
UNIVERSITY PRESS

Original article

Quantification of slip band distribution in polycrystals: an automated fast Fourier transform decomposition approach

Fernando D. León-Cázares,[1,2] Bradley Rowlands,[1] and Enrique I. Galindo-Nava[1,3]

[1] Department of Materials Science and Metallurgy, University of Cambridge, 27 Charles Babbage Rd, Cambridge, CB3 0FS, UK, [2] Sandia National Laboratories, 7011 East Avenue, Livermore, CA, 94550, USA and [3] Department of Mechanical Engineering, University College London, Torrington Place, London, WC1E 7JE, UK

Abstract

Plastic deformation is accumulated in slip bands in a wide variety of engineering alloys. Multiple material and loading conditions impact their distribution and degree of slip localisation, but these effects are rarely quantified. To tackle this, the current work introduces a fast Fourier transform (FFT) decomposition method and applies it to a tensile loaded polycrystalline nickel-based superalloy imaged via high resolution digital image correlation and electron backscatter diffraction. This approach identifies active slip planes over the FFT images of individual grains and performs inverse transforms such that slip band traces with shared orientations are isolated. This technique enabled the largest quantification of slip band spacings and in-plane strains to date, with a total of 6557 slip bands detected. The results show that the slip band spacings increase with grain size, with no evident dependence on grain orientation and Schmid factor. Slip bands are found to develop similar spacings along different octahedral planes and continue to spread over larger regions of the grain as the resolved shear stress of the active slip system increases. The FFT decomposition technique, which could be employed with multiple microscopy techniques, will allow for much needed large scale quantitative studies of slip localisation.

Key words: plastic deformation, slip band, slip localisation; slip planarity, fast Fourier transform, electron microscopy, digital image correlation, electron backscatter diffraction

(Received: xx xxxx xxxx; Revised: xx xxxx xxxx; Accepted: xx xxxx xxxx)

Introduction

Several structural metals and alloys accommodate plastic deformation in the form of slip bands. For example, these appear in face-centred cubic (fcc) materials with low stacking-fault energies, such as nickel-based superalloys (León-Cázares et al., 2020b) and some austenitic stainless steels (Kim et al., 2019; Li et al., 2021), and in hexagonal close packed metals like titanium (Guo et al., 2014) and zirconium (Andani et al., 2020). Slip bands are complex planar dislocation structures that develop along neighbouring slip planes, and are characterised by the presence of dipoles, multipoles, dislocation debris and other defects (Lukáš & Kunz, 2004; Risbet & Feaugas, 2008; León-Cázares et al., 2020b). Critically, slip is highly localised in these regions, which makes them preferential sites for crack nucleation (Sangid, 2013; Polák & Man, 2014; Stinville et al., 2015). Recent research (Stinville et al., 2022) has shown that the distribution of slip developed during the first cycle is indicative of the lifetime of polycrystalline materials under cyclic loading. Thus, there is a need to accurately characterise the slip band morphologies and distributions.

A plethora of factors affect the slip localisation behaviour. Slip bands form during the early stages of plasticity (Petrenec et al., 2014; Ho et al., 2015), and as deformation progresses,

the slip activity within them intensifies, their dislocation densities increase and additional bands form (Di Gioacchino & Quinta da Fonseca, 2015; Lavenstein et al., 2020). During cyclic loading regimes they often saturate after a number of cycles (Lukáš & Kunz, 2004; León-Cázares et al., 2020a), but the slip irreversibilities may continue to damage the microstructure (Mughrabi, 2009, 2013; León-Cázares et al., 2020a). Loading conditions such as temperature (Lerch et al., 1984), strain rate (Valsan et al., 1994) and strain amplitude (Kundu et al., 2019) influence the resulting slip band distribution and dislocation densities. Material properties that increase the slip planarity are low stacking fault energies (Risbet & Feaugas, 2008), and the presence of second-phases (Lunt et al., 2017) (particularly of smaller sizes (León-Cázares et al., 2020a)) and short range order (He et al., 2021; Kim et al., 2022; Abu-Odeh & Asta, 2022). Moreover, physical phenomena such as dynamic strain ageing (Aboulfadl et al., 2015) and hydrogen trapping leading to hydrogen embrittlement (Nibur et al., 2006; Ménard et al., 2008; Yu et al., 2019) have also been linked to more localised plastic deformation behaviours. However, while the literature concerning these matters has widely discussed the multiple roles of slip localisation, this is rarely done quantitatively and with a high statistical significance.

Slip bands can easily be observed with a variety of imaging techniques, from optical (Lerch et al., 1984; Lerch & Gerold, 1987; Valsan et al., 1994) to electron (e.g. with electron channelling contrast imaging (ECCI) (León-Cázares et al., 2020a),

digital image correlation (DIC) (Di Gioacchino & Quinta da Fonseca, 2013), etc.) and atomic force (Risbet et al., 2003; Risbet & Feaugas, 2008; Ménard et al., 2008) microscopy, albeit with different resolutions, or even combinations of these (Sperry et al., 2021). Some studies have manually quantified some of the slip band distribution parameters (Lerch & Gerold, 1987; Valsan et al., 1994; Risbet et al., 2003), but automating these measurements presents the following challenges:

(i) Accurately detecting the orientation of the slip band traces in each grain, as any reasonable measurement of their distribution must be taken perpendicular to them.

(ii) Quantifying the distribution of the slip bands with a particular orientation while ignoring the contrast of other features, such as second phases or non-coplanar slip bands.

(iii) Extracting real distances from the ones measured on the slip band projections at the sample surface.

Different techniques can be leveraged to overcome some of the above-mentioned challenges. High resolution digital image correlation (HR-DIC) and electron backscatter diffraction (EBSD) used in tandem in a scanning electron microscope (SEM), often employed to characterise slip band behaviour (Lunt et al., 2017; Jiang et al., 2017; Harte et al., 2020; Sangid et al., 2020; Stinville et al., 2020), provide all the geometrical information needed to assess their distribution. In spite of this, the quantification cannot be performed reliably mainly due to challenge (ii), as measurements for a given slip plane orientation become impossible due to the presence of other sources of contrast (the strain of slip bands with a different orientation in this case). Sperry et al. (Sperry et al., 2020) applied a Radon transfer to the HR-DIC dataset to automate the detection of slip bands, but manual verification still had to be done. Bourdin et al. (Bourdin et al., 2018) developed a Heaviside-DIC method that detects the discontinuities in the kinematic fields measured, and Charpagne et al. (Charpagne et al., 2020) further refined this technique by complementing it with Hough transforms and merging of contiguous and closely oriented steps, effectively capturing individual slip bands. However, this approach loses some spatial information (e.g. width of slip bands). Moreover, these approaches apply exclusively to DIC datasets. Alternatively, León-Cázares et al. (León-Cázares et al., 2020a) addressed the detection of slip bands by performing a fast Fourier transform (FFT) on ECCI micrographs, which effectively decomposes them into images each with the slip bands that share a single orientation. This enabled a more accurate quantification of slip band volume fractions in fatigue loaded nickel-based superalloys with different ageing conditions. However, the image processing was done manually, on just a few grains, on regions smaller than the grains and without the crystallographic information needed to overcome challenge (iii). Yet, this study showed the potential of FFT image decomposition, successfully employed in the past to deconvolute Kikuchi bands in Kikuchi diffraction patterns (Ram et al., 2014) and in other fields to measure varied feature shapes and orientations (e.g. (Ayres et al., 2008; Davis et al., 2012; Malek et al., 2013)), as a means to better characterise slip localisation.

The current work introduces a new automated technique to quantify the slip band distribution. The capabilities of this approach are demonstrated on a tensile loaded polycrystalline nickel-based superalloy. Challenges (i) and (ii) are tackled with a FFT that decomposes the strain data in a HR-DIC dataset into its components along different orientations, and challenge (iii) is addressed by incorporating the corresponding crystallographic data from EBSD. In return, this methodology outputs an extensive characterisation of slip band distribution across a sample. The results obtained provide a quantitative understanding of the slip localisation behaviour and new insights on the slip band formation and evolution in polycrystals.

Materials and methods

Material

This study was performed on the coarse-grained nickel-based superalloy RR1000, supplied by Rolls-Royce plc. Following powder processing to shape, the material was subject to a super-solvus solution treatment at 1170 °C/1 h, fan air cooled close to -1 °C/s, and then aged at 760 °C/16 h and static air cooled. The heat treatment implemented produces a uniform grain orientation distribution with mean planar grain diameter of 48.4 ± 18.2 μm including twins (obtained via EBSD). The microstructure is also known to correspond to a solid solution fcc γ matrix phase and two distinct families of the ordered $L1_2$ γ' phase, namely secondary and tertiary precipitates approximately 300 nm and 20 nm in size, respectively.

A dogbone tensile specimen was produced by electro-discharge machining, with a gauge length of 8 mm, width of 2 mm and thickness of 1 mm. Both surfaces of the sample were finished by grinding with 4000 grit paper. The surface for EBSD and HR-DIC image collection was further polished to 0.04 μm colloidal silica for 20 minutes.

Mechanical testing

An interrupted tensile test was performed on a 100 kN servo-hydraulic Instron machine at room temperature. A crosshead displacement rate of 8×10^{-3} mm/s was employed, which corresponds to a strain rate of 0.1 %/s, and the test was interrupted at a total strain of 2.1 %.

Full-field DIC

Full-field DIC to monitor the in-plane strains across the sample was performed on the reverse face to that used for EBSD and HR-DIC. A continuous white coating followed by a black speckle pattern, both of automotive flameproof paint, were applied via airbrush in multiple passes. Features were tracked in situ at 10 frames per second with an Imager E-Lite 1600×1200 px camera with a 100 mm fixed focal length lens, at a stand-off distance of 10 cm. This was enough to image the whole gauge length with a pixel size of 10 μm.

EBSD

An area of interest for EBSD and HR-DIC imaging of 3.98×0.18 mm^2 was defined at the centre of the gauge width. EBSD mapping was performed at a working distance of 8.5 mm on a Zeiss GeminiSEM 300, equipped with an Oxford Instruments EBSD detector and Aztec software version 3, to determine the crystallographic orientation of each grain. Image acquisition and stage movement were automated across 20 frames of 700×525 px^2, with 10 %

overlap per frame, needed to cover the area of interest plus a further ∼10 % padded area to ensure the HR-DIC dataset was fully contained. Acquisition was performed at 25 kV with a pixel size of $p_{EBSD} = 0.5$ μm and a dwell time of 4 ms/px.

HR-DIC

A surface pattern for HR-DIC imaging was applied through the reconstruction of a thin gold film following a method similar to that reported by Edwards et al. (Edwards et al., 2017) in TiAl and Di Gioacchino et al. (Di Gioacchino & Quinta da Fonseca, 2013) in an austenitic stainless steel. Sputtering was performed with an Emitech K550 sputter coater with a gold target, backfilled with argon to 0.1 atm and depositing at 20 mA for 25 s, resulting in a film approximately 2.5 nm thick. Subsequent remodelling was performed by heat treating at 300 °C/8 h in a water vapour atmosphere followed by a stabilisation heat treatment at 600 °C/24 h in fused silica ampoules under a vacuum of $< 5 \times 10^{-5}$ mbar. This pattern was masked when applying the airbrush speckles for full-field DIC.

HR-DIC image collection was performed ex-situ before and after loading in the Zeiss GeminiSEM 300. This was operated at 15 kV with a four quadrant Si-drift backscattered electron detector, found to give high atomic number contrast between the gold features and the superalloy substrate. To traverse the area of interest, the automated collection of approximately 400×12 frames was performed with the SmartStitch (Zeiss) software with 10 % overlap by moving the stage in a rectangular grid, defining a focal plane non coincident with the imaged plane. Individual frames had a field of view of 25.8×19.4 μm^2 with a pixel size of 12.6 nm, compared to the feature size of ∼ 30-80 nm. Images were recorded using a 60 μm aperture, with a dwell time of 13 μs/px and no noise reduction to 8 bit depth, attempting to match the brightness, contrast and working distance in pre- and post-test images. Fig. 1(a) shows an example of the speckle pattern recorded, where the feature sizes range between 3-8 pixels. A histogram of the pixel intensities across the area of interest is plotted in Fig. 1(b), indicative of a good contrast for image acquisition.

Individual HR-DIC images were stitched together with the FIJI stitching plugin, computing the optimal overlap, and employing linear blending in the overlap region. Stitching lines were not visible in this process. Owing to image correlation software memory limitations, the stitched images were divided into 8000×18000 px matched pre- and post-test frames, forming a grid of ∼ 100×1 frames with 10 % overlap covering the region of interest. Correlation was performed via least squares subset matching with the DaVis 8.4.0 (LaVision) software using a 21×21 px^2 subset size, 8 px step size between subsets and fitting second order deformation. Such image correlation routines output the u_i $(i = 1, 2)$ in-plane components of the displacement tensor across the defined area. The in-plane strains can then be calculated as

$$\varepsilon_{ii} = \frac{du_i}{dx_i} \quad (1)$$

and

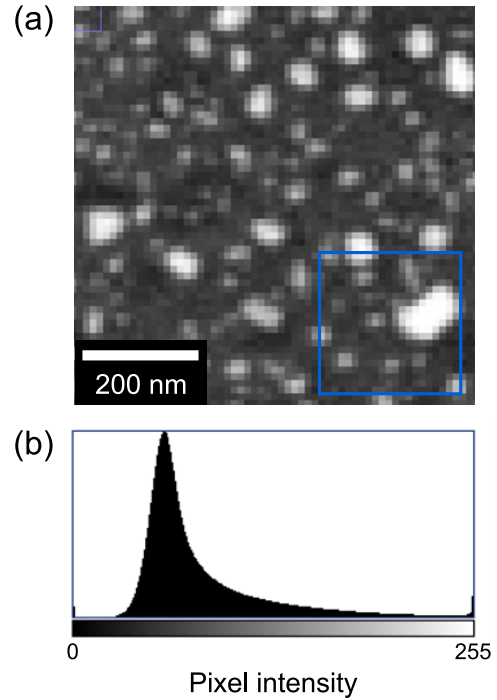$$\varepsilon_{12} = \frac{1}{2} \left(\frac{du_1}{dx_2} - \frac{du_2}{dx_1} \right) . \quad (2)$$

Fig. 1.: (a) Speckle pattern at imaging conditions showing the characteristic feature size. The box shows the subset size for image matching. (b) Histogram of pixel intensities across the area of interest, which contains few saturated pixels.

Results were visualised by plotting the maximum in-plane shear strain component, defined as

$$\gamma_{\max} = \sqrt{\left(\frac{\varepsilon_{11} - \varepsilon_{22}}{2} \right)^2 + \varepsilon_{12}^2} . \quad (3)$$

The pixel size used to match the distance between correlated displacement vectors, i.e. 8 raw image pixels, corresponds to $p_{DIC} = 100.7$ nm. The resulting strain fields were then merged again using the stitching plugin of FIJI to obtain a strain map of the full area.

To assess the non-random stitching artifacts, a small region without deformation was imaged and correlated by HR-DIC using the same steps. The largest strain variations introduced in this control test had a magnitude of ∼ 0.01. This is much lower than the strains detected along the slip bands (see the Results section), which proves the efficacy of the method at resolving these deformation features.

FFT decomposition method

The technique introduced in this section, denoted Fast Fourier Transform Decomposition (FFTD) (open source code available at [a]), makes use of the FFT to isolate the slip band information contained in the HR-DIC dataset. This allows for the decomposition of the contrast arising from differently oriented sets of slip bands. Table 1 summarises the steps followed. The corresponding scripts were coded into Matlab R2021a, making use of the image processing toolbox (IPT), the signal processing toolbox (SPT) and

---

[a]Source code for the FFTD technique: https://github.com/ferleoncazares/Slip-bands-FFT-decomposition

Table 1.: Summary of the preprocessing and FFT decomposition steps.

Preprocessing

Inputs: HR-DIC and EBSD datasets
Outputs: I^{B} and I^{G} images of each grain
1. Build binary and greyscale versions of DIC dataset
2. Merge EBSD and DIC datasets
3. Identify individual grains from EBSD dataset
4. Smooth and denoise grain boundaries
5. Topological analysis:
   - Sort grains by size
   - Compute rectangles enclosing each grain
   - Identify candidate grains that may be within a larger grain
   - Point in polygon algorithm in candidate grains to determine topology
6. Removal of DIC pixels near grain boundaries:
   - Boundary detection algorithm to remove outer pixels, repeat w^{-} times
   - Extend boundaries of inner grain boundaries and remove pixels, repeat w^{+} times
7. Crop DIC datasets to individual grains
8. Build masks of each grain with point in polygon algorithm
9. Apply masks to cropped binary images and skeletonise
10. Apply masks to cropped greyscale images

FFT decomposition

Inputs: I^{B} and I^{G} images of each grain
Outputs: $I^{IFFT(b)}$, slip band trace locations and angles
1. Perform FFT $\rightarrow I^{FFT,B}$ and $I^{FFT,G}$
2. Adjust contrast on $I^{FFT,B} \rightarrow I^{FFTd}$
3. Detection of active slip plane trace orientations:
   - Build spectrum of angular intensity in I^{FFTd}
   - Peak detection algorithm to determine the angles $\theta_s^{(b)}$ of b bright bands
4. Crop $I^{FFT,G}$ spectra for each bright band $\rightarrow I^{c(b)}$
5. Perform IFFT on $I^{c(b)}$ and apply mask $\rightarrow I^{IFFT(b)}$
6. Slip band detection:
   - Interpolate intensities in $I^{IFFT(b)}$ along search line at angle $\theta_q^{(b)}$ perpendicular to the slip bands
   - Peak detection algorithm to detect slip bands

the MTex 5.1.0 crystallographic toolbox (Hielscher & Schaeben, 2008; Bachmann et al., 2011). Relevant built-in functions used are referenced throughout the text.

Image preprocessing

A series of steps are needed to combine the EBSD and HR-DIC datasets in a meaningful way. The objective of the preprocessing stage is to create images of individual grains with HR-DIC strain-related data, each linked to their corresponding EBSD crystallographic information. Fig. 2 shows the different preprocessing steps.

Firstly, the EBSD and HR-DIC datasets need to be merged. Note that the sizes of the regions imaged by each technique are different, and so are their pixel sizes (denoted p_{EBSD} and p_{DIC}, respectively). For each EBSD frame, the coordinates of

approximately 30 triple junctions are manually collected in both coordinate systems. These are used to calculate the affine transformation and shift of the EBSD dataset giving the least squares differences to match those in the HR-DIC image (Atkinson et al., 2020; Harte et al., 2020). A maximum distance error of 6.8 EBSD pixels was obtained in the current study, and stitching lines were invisible without the need of smoothing filters. The grains, calculated using a threshold of $5°$ in neighbouring pixels, are then smoothed and denoised (smooth function in MTex) to better delimit their boundaries. Fig. 2(a) shows a region of the DIC image with superimposed grain boundaries calculated from the EBSD dataset.

A topological analysis is performed to determine which grains are fully contained within another grain as seen on the surface imaged. This will be helpful later, considering the large amount of twins in the material, to determine which pixels within the boundary of a grain must be ignored when performing the slip band analysis. The grains are firstly sorted by size, and the rectangles that contain them are computed from the minimum and maximum x and y coordinates of their pixels in the EBSD dataset. The grains with boxes that fully lie within that of a larger grain are considered candidates. A point in polygon algorithm (Hormann & Agathos, 2001) (inpolygon function in Matlab) is then used for an arbitrary pixel of each of the candidate grains to determine whether they are inside of the larger grain. This is illustrated in Fig. 2(b).

The DIC data near the boundary of each grain is removed from the analysis because of two reasons. Firstly, to avoid including pixels of neighbouring grains that may have been misplaced due to errors during the merging of the EBSD and DIC datasets. Secondly, because strain localisation behaviour and lattice rotation near grain boundaries vary substantially from those in the bulk of grains, and we are mainly concerned with the latter. To achieve this, a boundary detection algorithm (boundary function in Matlab) is performed on the EBSD data of the grain of interest, and the corresponding pixels are excluded. This step is repeated multiple times, for a combined width of w^{-} DIC pixels removed. Similarly, pixels within a layer of width w^{+} extended outwards from the grain boundaries of grains in the interior (polybuffer function in Matlab) are excluded. The removal of these layers of pixels in a grain is exemplified in Fig. 2(c).

Individual pictures can be built for each grain for the subsequent image analysis. A HR-DIC micrograph is cropped into the smallest rectangle of $X \times Y$ pixels that encloses the remaining EBSD data points of the grain of interest, as shown in Fig. 2(d), setting the new x and y coordinates of the bottom left pixel as $(1, 1)$. Masks $I^{mask} \in \{0, 1\}^{X \times Y}$ are constructed such that its elements ($x = 1, ..., X$ and $y = 1, ..., Y$) are

$$I_{x,y}^{mask} = \begin{cases} 1 & \text{if pixel } (x, y) \text{ belongs to the grain of interest} \\ 0 & \text{otherwise} \end{cases}.$$

(4)

These pixels are identified by first detecting on the EBSD data the boundaries of that grain and all grains inside of it, and then performing the point in polygon algorithm for every pixel of the cropped DIC image and each of these boundaries. The resulting mask can be applied to any image, i.e. multiplying the intensity of each of its pixels by the homologous one in I^{mask}. This can be done for any version of the HR-DIC figure, such as for different strain components or colouring formats (binary, greyscale or coloured).
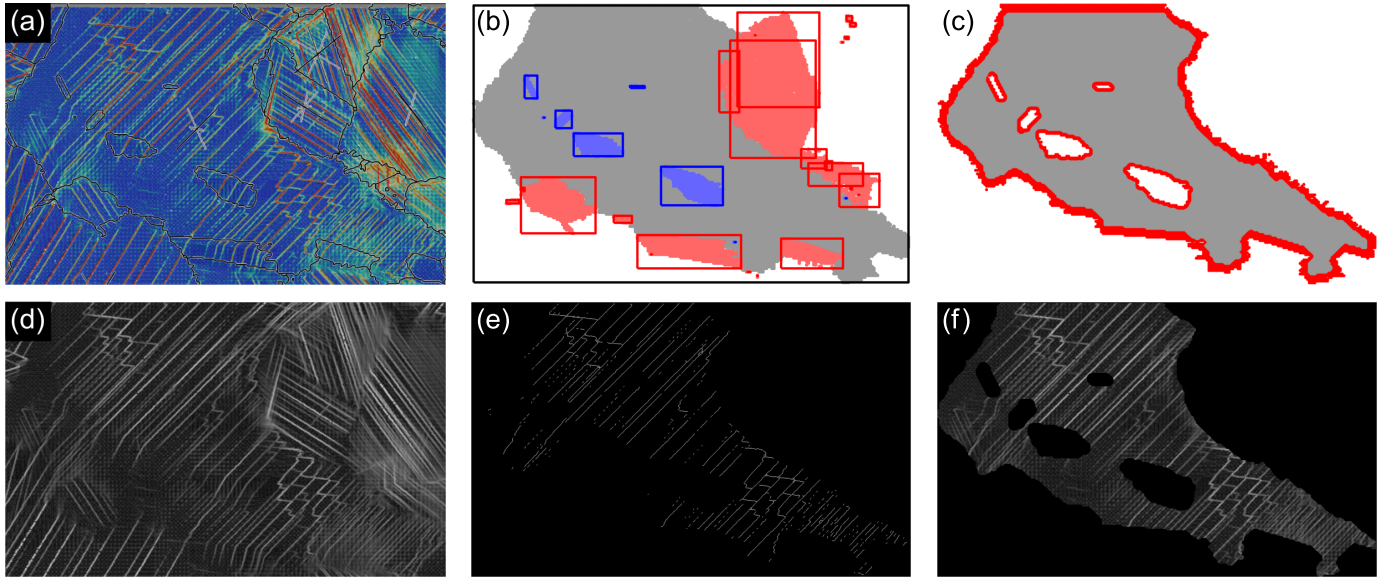
Fig. 2.: Steps of the preprocessing stage. (a) Matching of the EBSD and HR-DIC datasets, with superimposed grain boundaries calculated with the former and planar strains measured with the latter. (b) Grain topology, showing the candidate grains that do (blue) and do not (red) lie within the grain of interest (grey). (c) Regions near the grain boundary (red) excluded from the analysis. (d) Reduced version of the HR-DIC dataset, and (e) binary skeletonised and (f) greyscale images of the same region after applying the grain mask. The contrast of the greyscale images was adjusted for better visualisation.

Two versions of the DIC dataset are used in the following analysis. Firstly, a binary (pixel intensities of 0 or 1) image is created by setting a strain threshold $\gamma_{\text{th,B}}$ (maximum in-plane total shear strain in this work) such that many slip bands are evident and most regions in-between show no deformation. Afterwards, this image is skeletonised (`bwskel` function in the IPT), a standard operation that turns shapes, slip bands in the present case, into thin lines equidistant to their boundaries. Secondly, a greyscale (pixel intensities from 0 to 1) image is built such that pixels where the strains are above threshold $\gamma_{\text{th,G}}$ have an intensity of 1, and these linearly decrease until an intensity of 0 for no strain. The masks I^{mask} for each grain are then applied to these two versions of the DIC dataset to exclude the pixels that do not belong to them. This results in skeletonised and greyscale images of individual grains, such as those in Fig. 2(e) and (f), respectively.

FFT decomposition

The FFTD technique enables the detection of slip bands from the images generated in the preprocessing stage. Fig. 3 shows the steps followed to achieve this. Two-dimensional FFTs $\mathscr{F}$ (`fft2` function in Matlab) are applied to both the binary skeletonised $I^{\text{B}} \in \{0,1\}^{X \times Y}$ (Fig. 3(a)) and the greyscale $I^{\text{G}} \in [0,1]^{X \times Y}$ (Fig. 3(b)) images of individual grains; the former will later be employed to discern slip band orientations and the latter to detect slip bands. Such transforms ($\mathscr{F}\{I^{\text{B}}\} = I^{\text{FFT,B}}$ and $\mathscr{F}\{I^{\text{G}}\} = I^{\text{FFT,G}}$) of images in the space domain result in images $I^{\text{FFT,B}} \in \mathbb{C}^{X \times Y}$ and $I^{\text{FFT,G}} \in \mathbb{C}^{X \times Y}$ that contain the frequency components instead. Note that the intensity of pixel (x,y) for a given transform $\mathscr{F}\{I\} = I^{\text{FFT}}$ is computed as

$$I_{x+1,y+1}^{\text{FFT}} = \sum_{j=0}^{X-1} \sum_{k=0}^{Y-1} \omega_X^{jx} \omega_Y^{ky} I_{j+1,k+1}, \quad (5)$$

where ω_X and ω_Y are complex roots of unity

$$\omega_X = e^{-2\pi i/X} \quad (6a)$$

$$\omega_Y = e^{-2\pi i/Y}, \quad (6b)$$

and the zero-frequency component is then shifted to the centre of the spectrum (`fftshift` function in Matlab) at point (x_0, y_0) by swapping the first and third quadrants of I^{FFT} with the second and fourth.

The search for active slip planes is developed on an additional version $I^{\text{FFTd}} \in \mathbb{R}^{X \times Y}$ of the frequency spectrum. The intensity of each of its pixels is computed as

$$I_{x,y}^{\text{FFTd}} = |\log_2(I_{x,y}^{\text{FFT,B}})|. \quad (7)$$

The absolute value turns the pixel intensities to real numbers, as opposed to complex in $I^{\text{FFT,B}}$, and the logarithm serves to make the range of pixel intensities narrower, which helps for image readability. An example of this FFT is shown in Fig. 3(c). Each of the bright bands in the frequency domain captures a set of parallel slip band projections in the space domain.

A line search algorithm is implemented to spot the orientation of the brightest bands in I^{FFTd}. Pixel intensities $z_s(r_s, \theta_s)$ at radii r_s and angles θ_s are linearly interpolated from I^{FFTd} within a circle with radius of

$$R_s = \text{floor}\left(\frac{\min(X,Y)}{2} - 1\right) \quad (8)$$

pixels centred at (x_0, y_0), where the floor function rounds the value towards the nearest smaller integer and min is the minimum value function. The interpolation points are spaced one DIC pixel and $\Delta\theta_s$ degrees apart, for angles between $0° \leqslant \theta_s < 180°$.
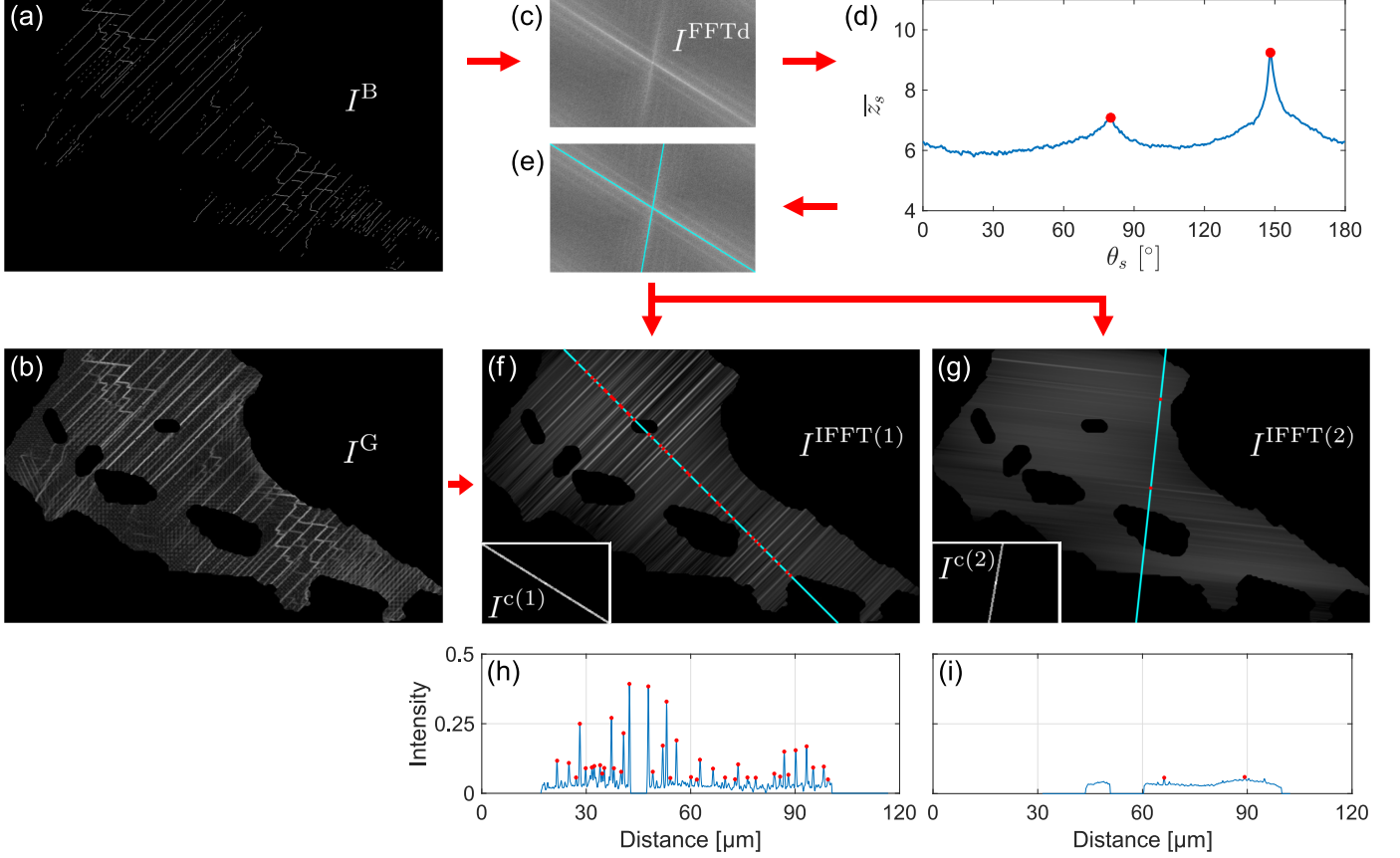
Fig. 3.: Steps of the FFTD shown for the same grain used in Fig. 2. (a) Binary skeletonised and (b) greyscale images of a grain. (c) Two-dimensional FFT of the binary image and (d) angular variation of the mean intensity with two peaks marked that correspond to the bright bands in the FFT, shown in (e). (f,g) IFFT performed on the two cropped versions of the FFT of the greyscale image (shown in the inserts), one for each active slip plane orientation. The search lines (cyan) and slip bands (red) detected from the (h,i) intensity profiles along them are displayed. The contrast of all greyscale images was adjusted for better visualisation.

The cartesian coordinates of the interpolation points are thus $(r_s \cos \theta_s + x_0,\ r_s \sin \theta_s + y_0)$. The mean intensity $\overline{z_s}(\theta_s)$ of interpolation points along one of these lines is computed as

$$\overline{z_s}(\theta_s) = (2R_s + 1)^{-1} \sum_{r_s=-R_s}^{R_s} z_s(r_s, \theta_s). \qquad (9)$$

An example of the angular variation of the mean intensity is shown in Fig. 3(d). A peak detection algorithm (`findpeaks` function in the SPT) with set minimum peak height $\overline{z_s}_{\min}$ and minimum peak prominence $\overline{z_s}_{\mathrm{rel}}$ is used on this spectrum to identify the angles $\theta_s^{(b)}$ ($b = 1, ..., B$) of the B brightest bands. This is shown back in I^{FFTd} in Fig. 3(e). It was found that adding to I^{FFTd} a two-dimensional Gaussian smoothing operation (`imgaussfilt` function in the IPT) with standard deviation σ_S before performing the pixel intensity interpolations reduces the noise of the $\overline{z_s}(\theta_s)$ spectrum, making the peak detection more consistent.

Excluding the pixels far away from a line at angle $\theta_s^{(b)}$ crossing through (x_0, y_0) in a FFT image effectively isolates the frequency components along that orientation. The distance $d^{(b)}(x, y)$ to that line can be calculated for a pixel situated at (x, y) as

$$d^{(b)}(x, y) = \frac{|m_s^{(b)}(x - x_0) - (y - y_0)|}{\sqrt{m_s^{(b)\,2} + 1}} \qquad (10)$$

(Bali, 2008), where $m_s^{(b)} = \tan \theta_s^{(b)}$ is the slope of the line. For each bright band b in $I^{\mathrm{FFT,G}}$, a cropped image $I^{\mathrm{c}(b)} \in \mathbb{C}^{X \times Y}$ is constructed such that

$$I_{x,y}^{\mathrm{c}(b)} = \begin{cases} I_{x,y}^{\mathrm{FFT,G}} & \text{if } d^{(b)}(x, y) \leqslant d^{\star}/2 \\ 0 & \text{otherwise} \end{cases}. \qquad (11)$$

Performing an inverse fast Fourier transform (IFFT) $\mathscr{F}^{-1}$ (`ifft2` function in Matlab) to these cropped spectra and applying the grain binary mask generates greyscale images $I^{\mathrm{IFFT}(b)} \in [0, 1]^{X \times Y}$ with slip bands of a single orientation that resemble those in the original image, i.e. $I^{\mathrm{IFFT}(b)} = \mathscr{F}^{-1}\{I^{\mathrm{c}(b)}\} \circ I^{\mathrm{mask}}$, where $\circ$ denotes an element-by-element matrix multiplication. The intensities of the individual pixels are calculated as

$$I_{x,y}^{\mathrm{IFFT}(b)} = \left| \frac{1}{X} \sum_{j=1}^{X} \frac{1}{Y} \sum_{k=1}^{Y} \omega_X^{(j-1)(x-1)} \omega_Y^{(k-1)(y-1)} I_{j,k}^{\mathrm{c}(b)} \right| I_{x,y}^{\mathrm{mask}}. \qquad (12)$$

Fig. 3(f,g) show the IFFT images computed from the two cropped spectra (displayed in the inserts), each for a different bright band in I^{FFTd}. Note that slip bands in the IFFT images may project beyond the grain boundaries if the binary mask is not reapplied (further details in the Discussion section). While this would not affect the detection of slip bands, the mask is reapplied here to facilitate the measurement of slip band spacings.

Measurement of slip band spacings

Slip bands can readily be identified from the IFFT images. Slip band volume fractions can be measured by selecting an intensity threshold, as done in reference (León-Cázares et al., 2020a). Instead, we focus our current efforts in quantifying the slip band spacings. For each bright band b in a FFT spectrum there is an associated line b in the space domain perpendicular to a set b of slip band projections that share a particular orientation. Thus, slip bands can be detected from the corresponding $I^{\text{IFFT}(b)}$. This is performed along the search line at an angle

$$\theta_q^{(b)} = \arctan\left(\frac{X}{Y}\tan\theta_s^{(b)}\right), \tag{13}$$

perpendicular to the slip bands and crossing through (x_0, y_0), although any other reference point could be chosen. The length in pixels $2R_q^{(b)} + 1$ of that search line is chosen to ensure that it goes through the whole image. Intensities $z_q^{(b)}(r_q^{(b)})$ at positions $r_q^{(b)} = -R_q^{(b)}, ..., R_q^{(b)}$ spaced one DIC pixel apart along that line are linearly interpolated from $I^{\text{IFFT}(b)}$, producing profiles like those in Fig. 3(h,i). Another peak detection algorithm, with set minimum peak height $z_{q\,\min}$, minimum peak prominence $z_{q\,\text{rel}}$ and minimum peak separation $r_{q\,\min}$, is then used to locate the positions $r_q^{(b,s)}$ ($s = 1, ..., S^{(b)}$) of the $S^{(b)}$ high intensity peaks detected along line b, which correspond to individual slip bands. The actual coordinates $(x_q^{(b,s)}, y_q^{(b,s)})$ of the points found are

$$x_q^{(b,s)} = r_q^{(b,s)} \cos\left(\theta_q^{(b)}\right) + x_0 \tag{14a}$$

$$y_q^{(b,s)} = r_q^{(b,s)} \sin\left(\theta_q^{(b)}\right) + y_0, \tag{14b}$$

with pixel intensities $z_q^{(b,s)}$. Note that these intensities are directly related to the HR-DIC strains used to build the greyscale image I^{G}, in-plane shear strains in this case. Such strains can be recovered as

$$\gamma_{\text{SB}}^{(b,s)} = z_q^{(b,s)} \gamma_{\text{th,G}}, \tag{15}$$

the physical meaning of which is further explained in the Discussion section.

With this data, the slip band spacings for each slip plane orientation spotted can be quantified. The peak-to-peak spacing between two adjacent slip bands are calculated as

$$\lambda^{(b,s)} = (r_q^{(b,s+1)} - r_q^{(b,s)}) \sin\alpha^{(b)} p_{\text{DIC}}, \tag{16}$$

where $\alpha^{(b)}$ is the angle between the sample surface (neglecting local height variations due to deformation) and slip plane b, as long as there are no pixels in-between that do not belong to the grain analysed (in which case this spacing is ignored). Similarly,

Table 2.: Parameters used in the image preprocessing and FFTD method.

Parameter		Value
Width of outer boundary excluded	w^-	5 p_{EBSD}
Width of inner boundary excluded	w^+	3 p_{EBSD}
Threshold for binarised image	$\gamma_{\text{th,B}}$	0.0375
Threshold for greyscale image	$\gamma_{\text{th,G}}$	0.35
Gaussian smoothing standard deviation	σ_S	1 p_{DIC}
FFT angle step size	$\Delta\theta_s$	0.05°
FFT spectrum minimum peak height	$\overline{z_s}_{\min}$	4.6
FFT spectrum minimum peak prominence	$\overline{z_s}_{\text{rel}}$	0.45
Width of cropped FFT	$d^\star$	3 p_{DIC}
IFFT profile minimum peak height	$z_{q\,\min}$	0.0457
IFFT profile minimum peak prominence	$z_{q\,\text{rel}}$	0.016
IFFT profile minimum peak separation	$r_{q\,\min}$	3 p_{DIC}

the mean linear slip band spacing (inverse to the linear slip band density) is

$$\overline{\lambda^{(b)}} = \frac{l^{(b)} \sin\alpha^{(b)} p_{\text{DIC}}}{S^{(b)}}, \tag{17}$$

where $l^{(b)}$ is the number of pixels that fall within the grain analysed along the search line b. The value of $\overline{\lambda^{(b)}}$ is slightly different and more accurate than that obtained by computing the mean value of all $\lambda^{(b,s)}$ in equation (16), which would not fully consider the slip bands nearest to the grain boundaries.

Finally, the orientation information can be recovered from the EBSD data. The angles of the slip band traces

$$\theta_{SB}^{(b)} = \theta_q^{(b)} + 90° \tag{18}$$

found via the FFT method are matched to those of octahedral planes predicted with the EBSD dataset (Gibson et al., 2021) by selecting the permutation that adds the smallest angle difference when considering all B active slip planes detected. Note that these differences must consider the cyclic nature of angles, e.g. a line at $-90°$ is equivalent to one at $90°$, and so forth. Once assigned, the $\alpha^{(b)}$ angles are related to the z-component $n_z^{(b)}$ (in-and-out of the sample surface) of the corresponding slip plane unit normals as $\sin\alpha^{(b)} = \sqrt{1 - n_z^{(b)\,2}}$. This is all performed using the mean grain orientations.

Parameter definition

This section outlines the parameters of the image preprocessing and analyses used in the current work, and how some of these were chosen. Table 2 displays such parameters.

Grains with less than two EBSD pixels were excluded from the beginning of the preprocessing stage because their effects on the slip band analysis were deemed negligible. A minimum of 1000 EBSD pixels, which corresponds to an area of $\sim 250\ \mu\text{m}^2$, was imposed after performing the grain topology analysis to determine which grains would be analysed. This threshold, set because the detection of bright bands in the FFT image becomes less consistent for smaller grains, was imposed both before and after removing the grain boundary layers (w^- and w^+).

For the slip band distribution analysis, the Gaussian smoothing of I^{FFTd} drastically minimises the false positive detections of
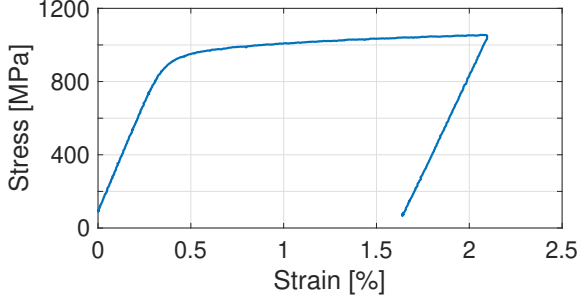
Fig. 4.: Stress-strain curve of the interrupted test.

Table 3.: Computing times and numbers of grains of the preprocessing and FFTD steps.

Step	Grains	Time [s]
Grain calculations and denoising	6369	445
Grain topology	3224	49
Removing grain boundary pixels	527	151
Building grain images	365	1240
FFT decomposition	365	240

bright bands, although nearby peaks become more likely to merge. Thus, σ_S was kept to a small value of 1 p_{DIC}. The FFT peak detection parameters were first chosen so that bright bands apparent to the naked eye were always detected, and the minimum peak prominence was set to avoid false positives from noise in the FFT. The width of the cropped FFT spectra was selected to produce IFFTs that resembled the original binarised images; a deeper analysis on the effects of this parameter are given in the Discussion section. The peak detection parameters to identify slip bands were chosen accounting for the background noise produced in the IFFT images. A value of 0.0457 was chosen for the minimum peak height, which corresponds to a strain of 0.016 in the original greyscale image, and the minimum peak prominence was adjusted manually to minimise the number of false positives encountered while including slip bands observed.

Results

The stress-strain curve of the alloy tested is plotted in Fig. 4. This shows that a plastic strain of about 1.64 % was achieved at the highest extension, but the strain is distributed heterogeneously across the sample. Fig. 5(a) shows that the axial strain, obtained via full-field DIC, is distributed evenly across the gauge length of the sample, but has a degree of heterogeneity at the sub-millimetre length scale. However, part of the strain fluctuations observed must be attributed to noise associated to DIC, e.g. from lens aberrations. The EBSD of the area of interest, enclosed in a rectangle in Fig. 5(a), is shown at a higher magnification in Fig. 5(b). Note that this area is considerably larger than that used in most HR-DIC studies. A subregion of this area is displayed at a larger magnification in Fig. 5(c), where individual grains and twins can be discerned. The HR-DIC image of this subregion, Fig. 5(d), shows that most of the plastic strain in the material is accumulated in slip bands, with a clearly heterogeneous distribution across grains. It is this slip band distribution which our new FFTD technique quantifies.

The preprocessing and FFTD took a total of 35.4 minutes; Table 3 shows the times taken to compute the different steps of this methodology. All calculations were run sequentially in a personal computer. The majority of the time was spent building the images of individual grains, for the most part performing the point in polygon algorithm to assign the DIC pixels of each grain.

The numbers of slip bands detected per grain vary considerably. A total of 6557 slip bands are distributed amid 365 grains analysed. This is, to the knowledge of the authors, the largest quantification of slip bands in a single sample to date. The grains have varied numbers of active slip plane orientations, as shown

in Fig. 6(a), with the majority displaying two distinct ones. Fig. 6(b) shows the distribution of slip bands based on the type of slip plane, where that associated with the brightest band in each FFT image is denominated primary slip plane, the second brightest secondary, and so on. This demonstrates that brighter bands in FFT images are the result of higher numbers of slip bands with a shared orientation.

The orientations of the slip band traces θ_{SB} detected with the FFTD method resemble those of octahedral planes calculated with the EBSD data θ_{EBSD}, but there are some deviations. The angle differences $\Delta\theta = \theta_{SB} - \theta_{EBSD}$ show a mean absolute error of $2.1°$ and some individual deviations above $9°$. The highest angle differences per grain, plotted in Fig. 7(a) as a function of the crystallographic direction in-and-out of the sample surface in an inverse pole figure (IPF), show systematic deviations for particular grain orientations. For example, large positive errors consistently appear for orientations between $\langle 001 \rangle$ and $\langle 011 \rangle$. Additionally, upon visual inspection, slip plane traces drawn with the angles obtained via FFTD closely follow the slip bands in the micrographs. These two hints indicate that there was a misalignment when obtaining the EBSD data. Thus, we performed an optimisation algorithm to determine the rotations by the Euler angles along the z, x and z-axes that the crystals as detected by EBSD would have to undergo to minimise the angle differences. A small rotation of $4°$ resulted in the angle differences shown in Fig. 7(b), with a mean absolute error of $0.55°$ and 99% of the individual angle differences below $2.5°$. Fig. 7(c) shows the histograms of the angle differences for the original and optimised orientations, indicating a considerable improvement. Moreover, Fig. 7(d) plots the mean angle differences and standard deviations for the primary, secondary and tertiary slip planes. The errors are clearly lower on the former, indicating that the FFT band detection algorithm improves when more slip bands are visible.

The above analysis returned five instances of active slip planes with traces that did not match any of those predicted by EBSD. Further inspection revealed that one of those false positives was due to the detection of slip bands from a neighbouring grain that the preprocessing grain boundary removal operation (w^-) did not eliminate. Two more were detections of slip bands in a small twin within the grains of interest, with clear signs of slip band transmission through the twin boundaries, that was not indexed by the EBSD. Another case occurred due to high strains near a grain boundary above the threshold $\gamma_{\text{th,B}}$, which introduced an artifact in the skeletonised version of the grain image. Lastly, a false positive was obtained in the grain shown in Fig. 8. The bands indicated correspond to what is often referred to as wavy slip, a zig-zag pattern that arises from the sequential activation of dislocations on two slip planes. This may affect the slip band detection algorithm only
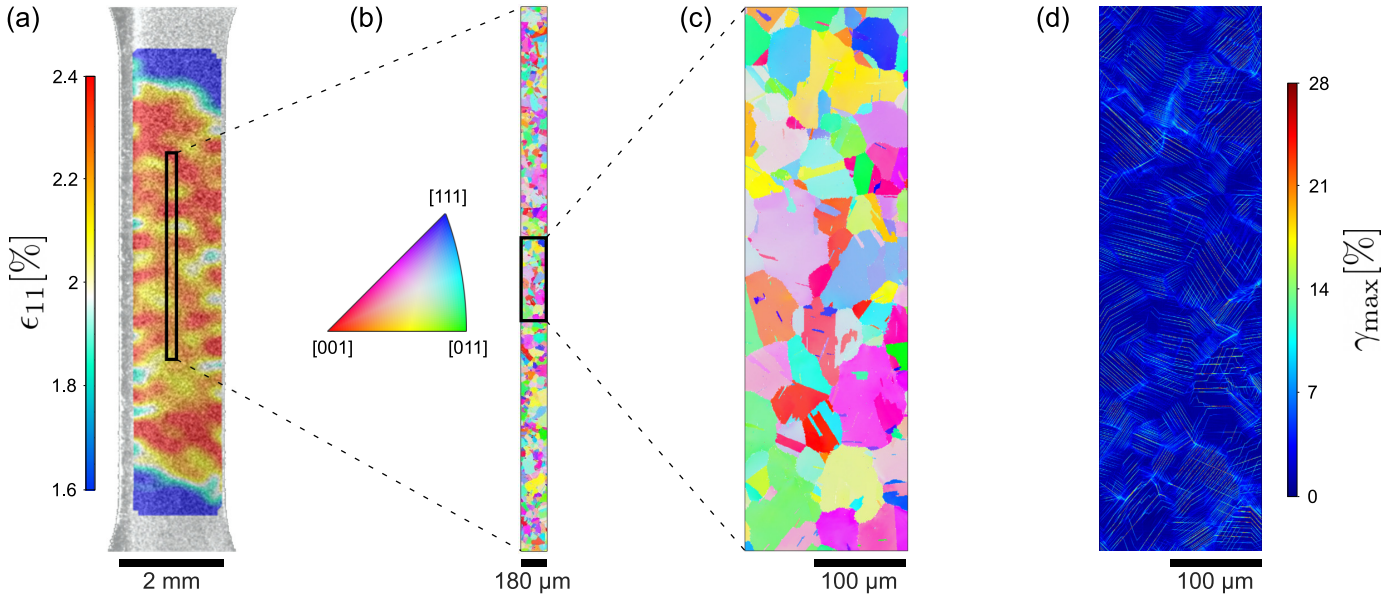
Fig. 5.: (a) Full-field DIC displaying the axial strain at the highest extension of the sample. (b) Pre-test EBSD of the area of interest (colour coded according to the crystallographic direction normal to the sample surface), and (c) EBSD and (d) post-test HR-DIC of a subregion shown at larger magnification. The full-field DIC was performed on the opposite face to that used for EBSD and HR-DIC.
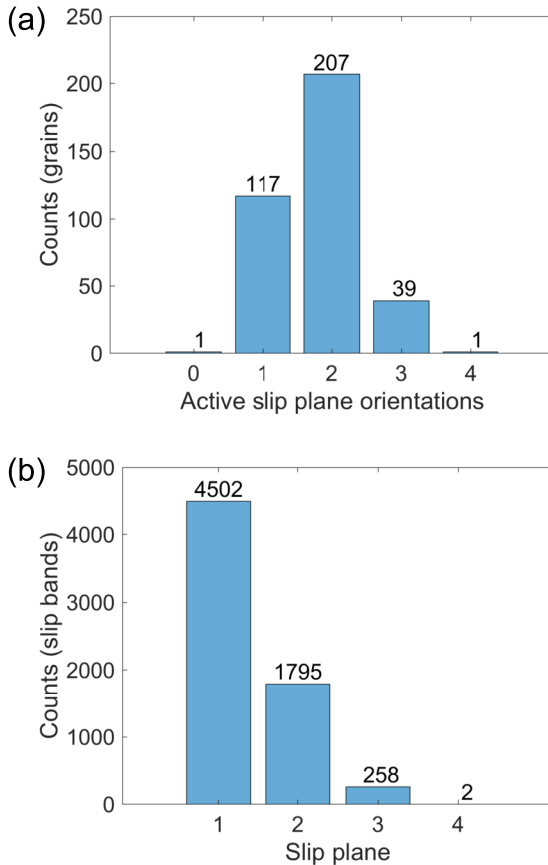

Fig. 6.: Numbers of (a) grains with 0, 1, 2, 3 and 4 active slip plane orientations as detected from the bright bands in the FFT images, and (b) slip bands detected in primary, secondary, tertiary and quaternary slip planes. The individual counts are shown above each bar.

when the period of the zig-zag pattern is close to the pixel size; otherwise, the FFTD method is capable of discerning the active slip planes (see Fig. 3). These false positives were removed from all the quantitative analyses in the current work.

The FFTD algorithm distinguishes closely oriented slip band traces from the FFT images. The minimum angular separation detected was $7.1°$. However, it is not clear whether slip band traces closer than that can be accurately differentiated. Fig. 9 shows the minimum angular difference between the traces of all octahedral planes in an fcc crystal calculated as a function of the surface normal direction. Two non-coplanar slip planes develop similarly oriented traces when the surface normal falls near the $\langle 001 \rangle$-$\langle 111 \rangle$ or $\langle 011 \rangle$-$\langle 111 \rangle$ edges of the IPF. However, from the 10 grains with the closest slip band traces found, also plotted in Fig. 9, only two had a surface normal further than $10°$ away from a $\langle 001 \rangle$ orientation, for which there are two pairs of octahedral planes with equal traces. This occurs because the two slip planes that share a trace orientation possess active slip systems with similar Schmid factors, which happens more consistently for orientations in this region of the IPF. Fortunately, in grains with a $\langle 001 \rangle$ surface normal, those two slip planes are also positioned at the same angle α from the sample surface. Thus, any FFT band detection error would affect the true slip band spacings measured (equations (16) and (17)) to a small extent. Measurements will only be affected largely if both planes develop slip bands such that their traces cannot be distinguished.

A mean slip band spacing of 1.85 μm was measured across all primary slip planes of the grains analysed, but individual values varied considerably. Fig. 10(a) shows the distribution of mean spacings across grains calculated with equation (17), although it must be taken into account that some grains have considerably more slip bands than others. More defined profiles that resemble log-normal distributions appear in Fig. 10(b) when considering
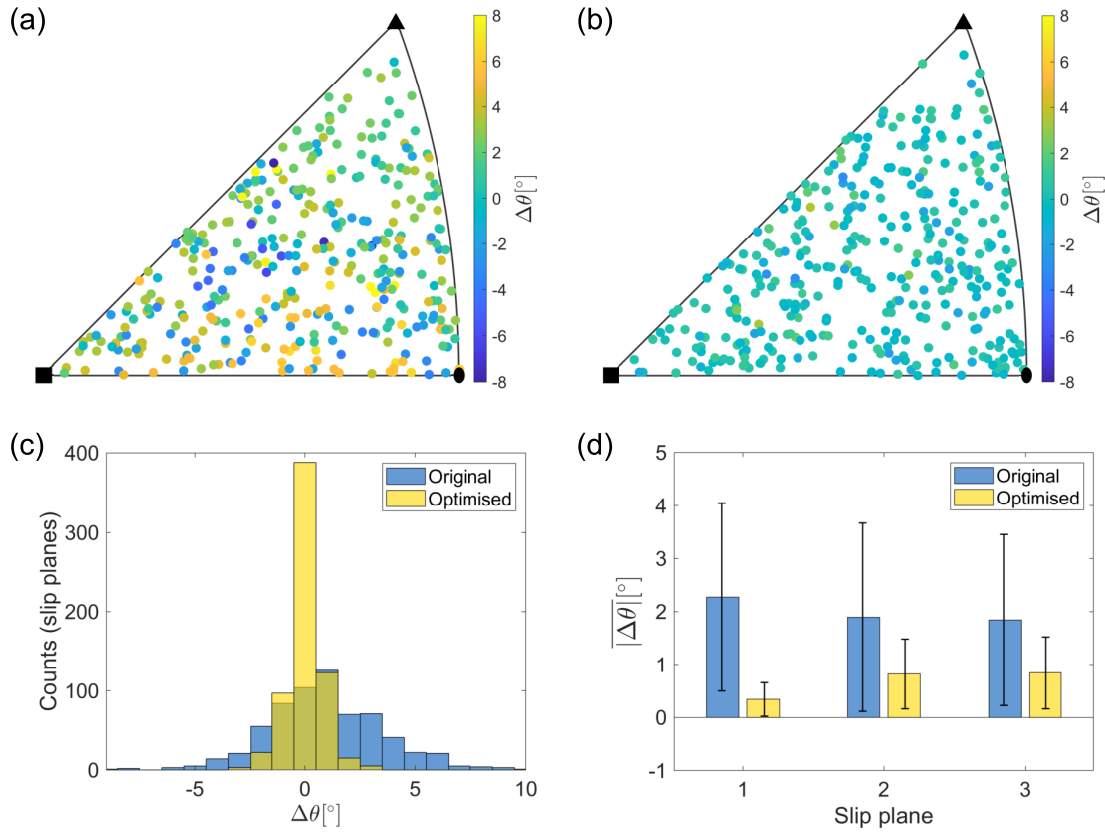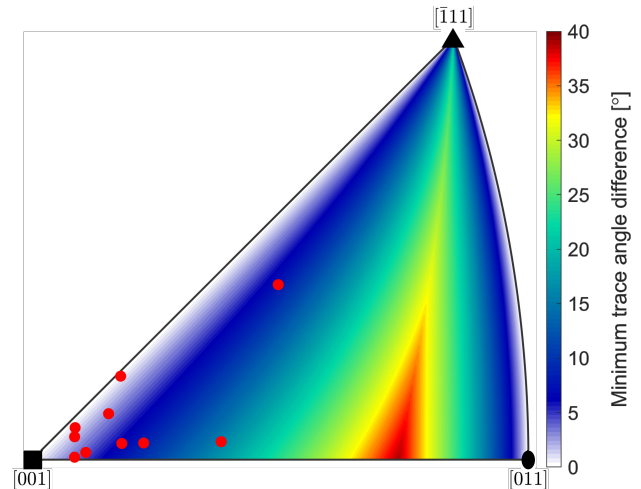
Fig. 7.: FFTD and EBSD trace angle differences shown as a function of the surface normal for the (a) original and (b) optimised orientations. (c) Histograms of the angle differences, and (d) their means and standard deviations (half error bar) along primary, secondary and tertiary planes for the original and optimised orientations.
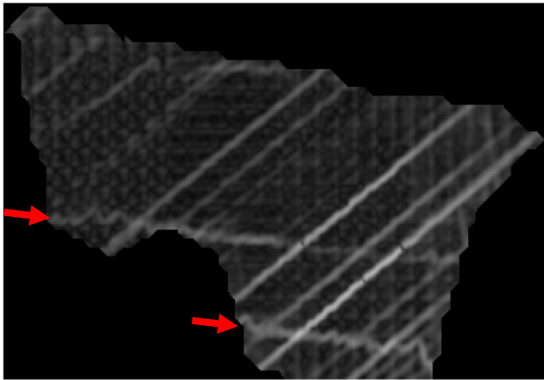
Fig. 8.: Grain where a false positive due to wavy slip was identified. The arrows point at two deformation bands with the characteristic zig-zag pattern of wavy slip. The contrast of the image was adjusted for better visualisation.

Fig. 9.: Minimum trace angle difference between octahedral planes of an fcc crystal as a function of the surface normal. The 10 grains with the more closely aligned slip band orientations detected are plotted.

the 5756 individual spacings measured with equation (16) between contiguous slip bands.

The large number of slip bands detected allows us to analyse the dependence of the spacings on other variables. For instance, a large scatter in slip band spacings is immediately observed for smaller grain sizes in Fig. 10(c). The dashed line, which represents a linear regression taking into account all the spacings measured (not only the mean values per grain), has a positive slope with

a high statistical significance (low p-value). This indicates that, on average and despite the scatter, shorter spacings are achieved in smaller grains down to the size threshold used in this study.
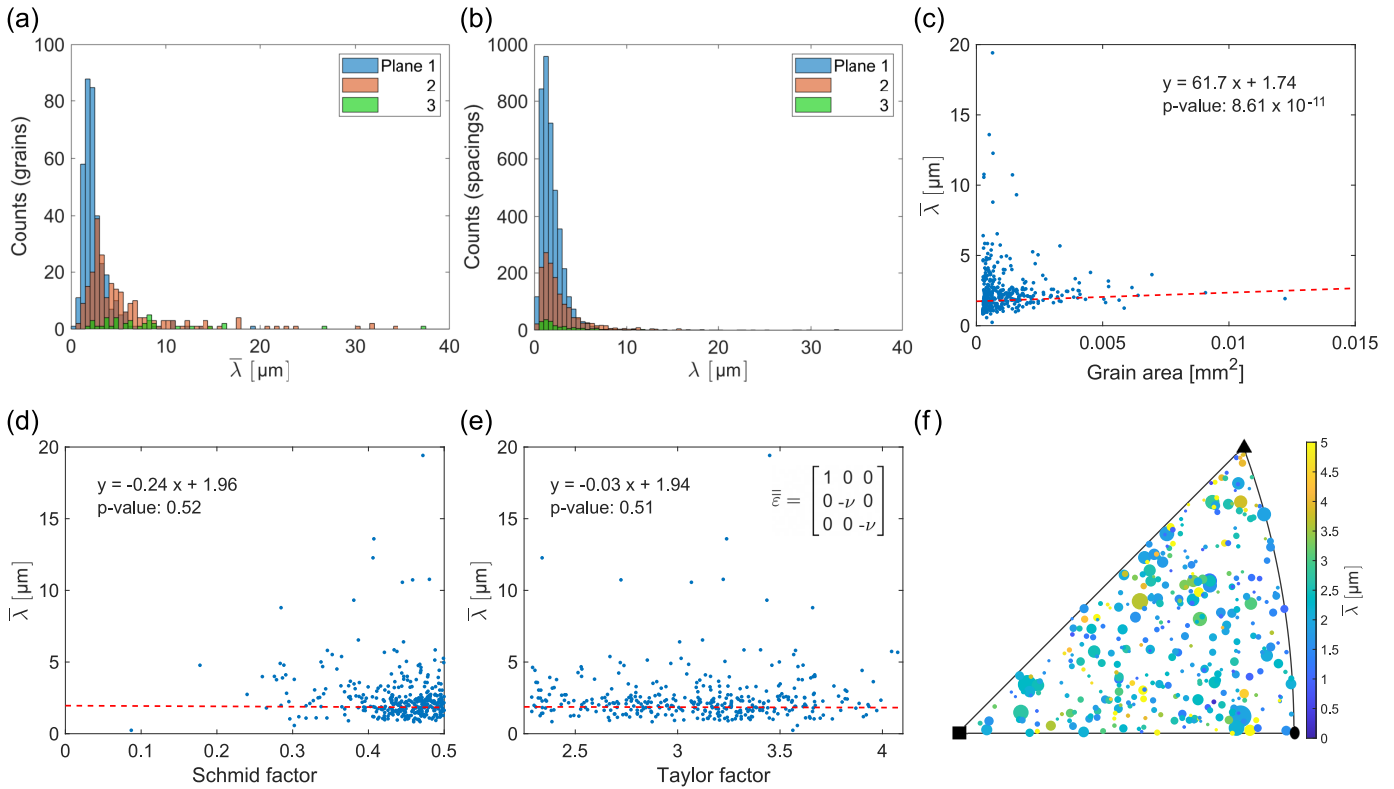
Fig. 10.: Histograms of the (a) mean slip band spacings per grain and (b) individual spacings along different slip planes. Mean slip band spacings on primary planes as a function of (c) grain area, (d) Schmid factor, (e) Taylor factor and (f) loading direction. The dotted lines in (c), (d) and (e) correspond to linear regressions taking into account all the spacings measured, with the equations and p-values shown. The strain tensor assumed to calculate the Taylor factors is indicated in (e), with $\nu = 1/3$. Larger marker sizes in (f) correspond to bigger grains.

Fig. 10(d) explores the effect of the uniaxial loading Schmid factor (using the highest value for the corresponding slip plane). As expected, low values result in more widely spaced slip bands because dislocations experience lower shear stresses. However, unlike in the previous case, a linear regression shows a very poor statistical significance. A comparably low correlation is shown in Fig. 10(e) with respect to the Taylor factor. This means that there is no clear dependence of the slip band spacing on any of these geometric parameters. A similar lack of trend is obtained if plotted against other stress components (e.g. Escaig or normal stresses (León-Cázares & Rae, 2020)). It is also hard to distinguish any pattern when plotted against the grain orientation, as seen in Fig. 10(f).

A similar analysis can be performed on the slip band strains measured with the FFTD approach. The distribution of mean slip band strains $\overline{\gamma_{SB}^{(b)}}$ per grain and plane orientation as detected from the IFFTs is shown in Fig. 11(a). These resemble Gaussian distributions where, as expected, strains are larger on primary slip planes. Note that no values under 0.016 appear due to the minimum peak height chosen for the slip band detection algorithm. If such low strain slip bands were considered, these distributions would shift towards lower values. Fig. 11(b) shows the distribution of slip band strains measured across the whole sample. All the distributions have a large number of low strain slip bands, but those on secondary and tertiary planes decrease more steeply. We refrain from showing additional dependences of the recorded

strains by reminding the reader that these are only in-plane strains. True three-dimensional values could only be recovered if the main Burgers vector of the dislocations that form each slip band was known.

Discussion

The results of the methodology introduced offer a new picture of how the plastic deformation, localised in the form of slip bands, is distributed across the grains of a polycrystal. However, the results obtained are not definite properties of the material, which are impossible to obtain because of two main reasons. Firstly, the detection of slip bands is affected by the resolution of the HR-DIC, and the FFTD and peak detection parameters. Edwards et al. (Edwards et al., 2017) showed by performing DIC of an area with different subset sizes that what appears to be a single slip band may actually be a collection of thinner bands. Secondly, even if a perfect resolution and slip decomposition could be achieved, the very concept of slip band is often ill-defined. For instance, it is not clear when some form of planar slip can be named a slip band; it could be a single dislocation pile-up, two of them in close proximity to each other (which still requires arbitrarily selecting a maximum separation distance) or more. Similarly, it is not always clear where a slip band ends and another one begins (León-Cázares et al., 2020b), so the same dislocation structure could be classified as two thin slip bands or as a single thicker one. Despite these caveats,

(a)

(b)
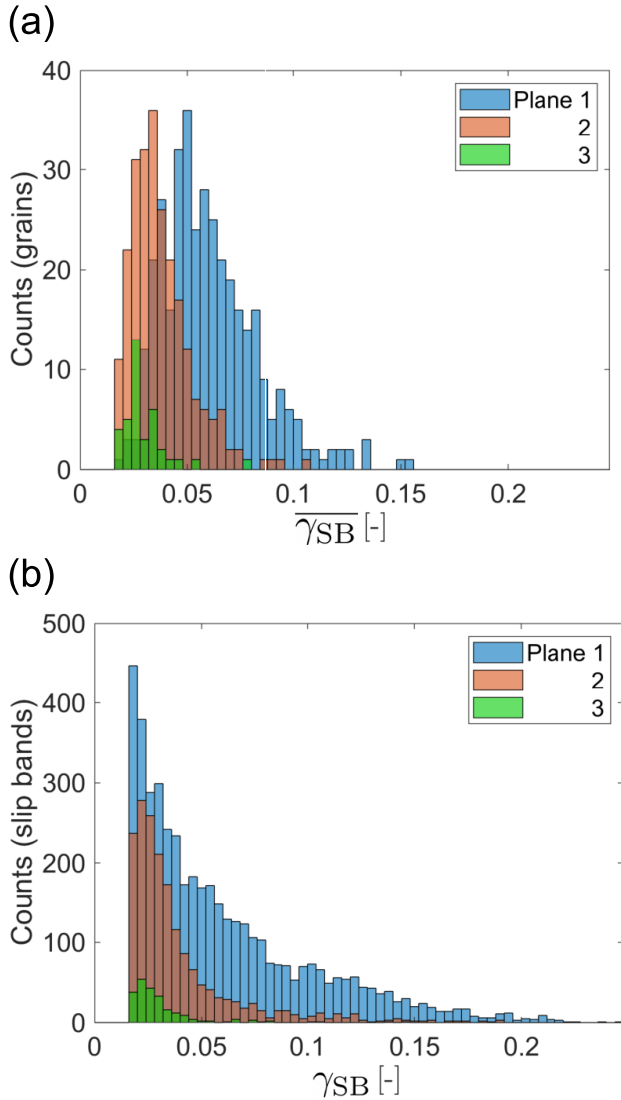
Fig. 11.: Histograms of the (a) mean slip band in-plane shear strains per grain and (b) individual measurements along different slip planes.

we argue that the FFTD does capture important aspects of the slip localisation behaviour in the material. Moreover, it will detect the differences in slip band spacings and strain profiles if performed on different samples using the same microscopy setups and FFTD parameters, allowing for direct quantitative comparisons.

Another point that needs to be discussed is the physical meaning of the slip band strains recorded after performing the FFTD. For this, a comparison between the slip band strain profiles in an original grain image (I^{G}) and its corresponding IFFT ($I^{\mathrm{IFFT(b)}}$) decompositions is shown in Fig. 12(a-e). The pixel intensities for each slip band were interpolated from these images along lines at angles $\theta_{SB}^{(b)}$ that go through points $x_q^{(b,s)}$ and $y_q^{(b,s)}$, equations (18), (14a) and (14b), respectively. In all cases, the strain profiles obtained from the IFFTs (red) closely follow those in the original image (blue), although with smoother curves. While not exactly moving averages, every point along one such profile is affected by the contrast of nearby pixels on the slip band. Nonetheless, a considerable advantage is that the strain profiles from IFFTs exclude

the peaks that develop when the slip band of interest intersects other features, such as non-coplanar slip bands in this example. Fig. 12(f) illustrates this in more detail. These findings imply that slip band strains can be estimated more reliably using the FFTD approach. The strains $\gamma_{\mathrm{SB}}^{(b,s)}$ calculated with equation (15) are fully decoupled from sources of contrast in the image other than the slip band in question.

However, it must be noted that the strains recorded are affected by the FFT cropping width $d^\star$ chosen, which determines the frequency components recovered upon performing the IFFT. A parametric analysis of this variable is performed to better understand its effects on the slip band profiles in the space domain. An original greyscale image of a grain in Fig. 13(a) is shown side by side with the recovered IFFTs on a secondary slip plane using different values of $d^\star$, Fig. 13(b-d). The corresponding strain profiles of the slip band pointed at by the arrows are compared in Fig. 13(e). The profile of this slip band, which starts at a grain boundary and disappears as it approaches the centre of the grain, is displayed as a decreasing slope from the left followed by intensity peaks that correspond to its intersections with non-coplanar slip bands. However, when a value of $d^\star = 1\ p_{\mathrm{DIC}}$ is used, Fig. 13(b), this slip band extends through the entirety of the grain with an almost constant contrast. By preserving a single line of pixels from the FFT image, the resulting IFFT can be thought of as a one-dimensional transform. For larger values of $d^\star$, Fig. 13(c,d), the shorter slip band is recovered thanks to the contributions of frequency components slightly misaligned with the FFT bright band. Yet, these components also introduce artifacts in the form of intensity oscillations further along the slip band profile. Generally, such artifacts become smaller for more homogeneous slip bands, which develop more prominently on primary slip planes.

The results obtained offer insights into the heterogeneous distribution of plastic deformation across the sample. Slip bands are on average further spaced apart in larger grains, as shown in Fig. 10(c). A similar finding was reported in 316L stainless steel over a smaller dataset (Ménard et al., 2008). This phenomenon is likely an effect of the grain boundaries, which often develop larger stresses in their vicinity compared to those in the grain interiors as a consequence of strain partitioning (Fallahi & Ataee, 2010). It is the larger von Misses stresses developed in alloys with smaller grain sizes which ultimately give rise to the Hall-Petch relationship (Ospina-Correa et al., 2021). Thus, smaller grains in the polycrystal may develop larger stresses on average, resulting in the shorter mean slip band spacings observed. Despite this rationale, the way in which our approach performs the quantification must also be taken into account. Slip bands are detected along lines that cross the grains near their centres, which in bigger grains are overall further away from grain boundaries. The trends reported are those towards the grain interiors, which in bigger grains have stresses that deviate more from those near the grain boundaries.

Moreover, the stress orientation does not show a clear effect on the slip band statistics. Low Schmid factors promote larger slip band spacings, but no significant variation is observed overall. In addition to the linear regression shown in Fig. 10(d), we performed a Spearman correlation test, i.e. a nonparametric measure of rank correlation that does not assume any particular functional dependence between the variables. The Spearman's rank coefficient of 0.0566 indicates only a very weak correlation, consistent with the previous findings. The same conlusion is reached when
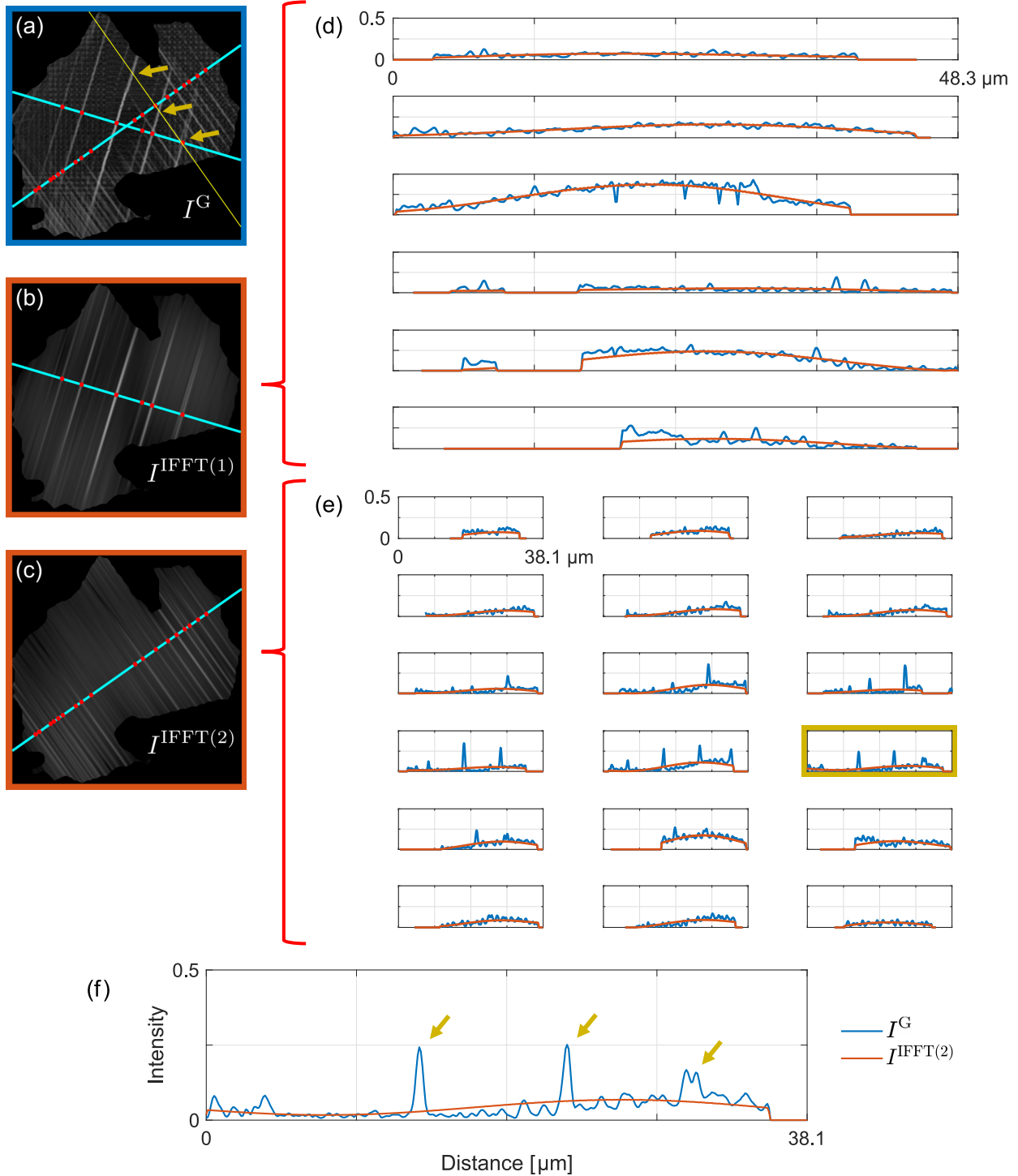
Fig. 12.: (a) Greyscale image of the planar strain in a grain and (b,c) its corresponding IFFT images for each active slip plane orientation. The search lines (cyan) and slip bands detected (red) are plotted. (d,e) Pixel intensity profiles along each of the slip bands detected in both images. The slip band highlighted in (a) and its profiles enclosed in (e) are shown in more detail in (f). Arrows pointing at the peaks in intensity correspond to the slip band intersections indicated in (a), sources of contrast external to the slip band of interest that do not appear in the IFFT image. The contrast of the greyscale images was adjusted for better visualisation.
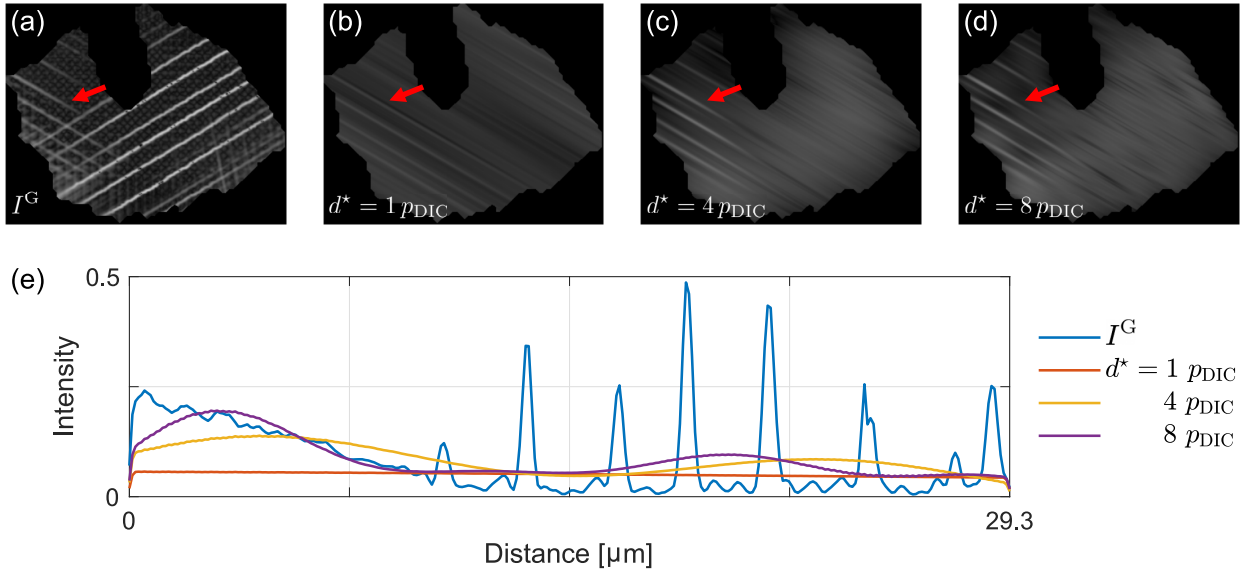
Fig. 13.: (a) Greyscale image of the planar strain in a grain, and secondary slip IFFT images generated by the FFTD method using cropping widths $d^\star$ of (b) 1 p_{DIC}, (c) 4 p_{DIC} and (d) 8 p_{DIC}. The arrows point the same slip band, with strain profiles plotted in (d). The contrast of the greyscale images was adjusted for better visualisation.

analysing the Taylor factor. A similar behaviour, although considering mean grain strains instead, was reported in a previous study in nickel-based superalloys (Harte et al., 2020). This lack of a clear correlation can be explained by acknowledging that the deformation distribution is a function not only of grain orientation, but also of the configuration of neighbouring grains. The local arrangements of differently oriented grains promote strain partitioning across the material. Neighbourhoods of grains can show collective behaviours based on their intrinsic properties and topological connectivities (Mangal & Holm, 2018). An example of this is seen in Fig. 14, which shows the grains imaged coloured according to the mean slip band spacings on their primary planes. Two regions, pointed at by the arrows, contain multiple contiguous grains with statistically large slip band spacings. Factors that influence this collective behaviour are the differences in stiffness and Schmid factor of neighbouring grains. Birosca (Birosca, 2015) showed in superalloy RR1000 that this results in the formation of soft and hard grains, with very different deformation behaviours as shown by the distributions of their geometrically necessary dislocations. Moreover, slip transfer across individual grain boundaries also plays a big role in the redistribution of slip. Multiple cases of slip band transmission, which effectively provide slip bands in highly stressed grains with long-range influence in their vicinities, were observed in the region imaged. All these phenomena introduce heterogeneous stresses across the material making the mesoscale deformation not crystallographic in nature, thus reducing the relevance of crystal orientation and Schmid factor as predictors for the slip band distribution in a given grain.
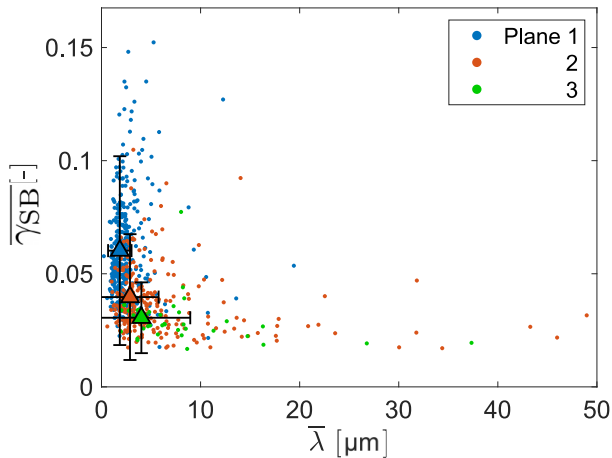
While only a time frame was captured, the large dataset captured allows us to better understand the evolution of plastic deformation. The distributions of individual slip band spacings on secondary and tertiary slip planes have similar modes to that on primary ones, but a larger one when considering the mean spacings per grain (Fig. 10(a,b)). Note the difference on how these distances are measured, i.e. equations (16) and (17). Moreover, the

modes and domains of the strain distributions are similar across all active slip planes (Fig. 11(b)), but the proportion of slip bands with a higher strain is considerably larger on primary ones. These trends indicate that, during the initial stages of plasticity, slip bands develop in localised regions with characteristic spacing distributions. As the resolved shear stress increases, these slip bands spread into larger regions of the grain, likely via a double cross-slip mechanism (Koehler, 1952; León-Cázares et al., 2020b). As this happens, the amount of plastic deformation per slip band increases unevenly. Once slip bands occupy the entirety of the grain, more of these become increasingly active, shifting the mean strains measured towards higher values. This occurs because the most active slip bands approach a level of strain saturation, forcing additional bands to accumulate more plastic deformation. These steps later develop on secondary and tertiary slip planes. Statistically, these develop similar slip band spacings over smaller regions and with a lower fraction of high strain slip bands due to the lower stresses attained.

Important aspects of the slip localisation behaviour are also captured in this dataset, despite not fully quantifying the amount of slip per slip band. Such a measurement would need to include three-dimensional strains, not available from DIC, and the quantification of slip band widths, which we consider unviable with the resolution employed and qualitatively appears to vary to a lower degree. Fig. 15 shows the recorded mean slip band spacings and in-plane strains per grain, as well as the overall means and standard deviations from individual measurements. The larger resolved shear stresses on the primary planes promote shorter slip band spacings and larger strain levels to accommodate the additional deformation. Mapped in a plot like this, grains, alloys and loading conditions with more planar slip would manifest further to the top right for equal amounts of plastic deformation. This approach could facilitate much needed large scale quantitative studies of slip planarity, with potential applications in the study

Fig. 14.: Grains coloured by the mean slip band spacings on their primary planes. White regions correspond to grains smaller than the size threshold, not analysed with the FFTD technique. The two arrows point at regions where multiple contiguous grains have large mean slip band spacings.

Fig. 15.: Map of the recorded mean slip band in-plane shear strains and spacings per grain on primary, secondary and tertiary slip planes. The overall means from the individual measurements are plotted as triangles, together with their standard deviations (half error bars).

the slip directionality. More importantly, the FFTD is not limited to DIC datasets. For instance, a simpler approach proved useful on ECCI (León-Cázares et al., 2020a), which detects slip bands using a very different source of contrast. Thus, we believe the FFTD could also be applied to other types of micrographs. At a larger length scale, it could potentially be used to quantify slip band distributions quickly and over large areas using optical microscopy. Upon adding the crystallographic orientation information via EBSD or alternative techniques like directional reflectance microscopy (Gaskey et al., 2020), the FFTD approach could be applied to any technique that can consistently detect slip bands.

Conclusions

A novel methodology was developed to automate the quantification of the slip band distribution in polycrystalline alloys. The slip band projections are identified from HR-DIC micrographs and the crystal orientations detected via EBSD. Performing FFTs of individual grain images, followed by IFFTs along independent directions, effectively decomposes the original strains observed into images each with the slip bands that share a single orientation. From these, slip band spacings and in-plane shear strains can be measured.

The application of this technique on a tensile loaded polycrystalline nickel-based superalloy returned the largest slip band quantitative analysis to date. The distributions measured indicate that slip bands are on average further spaced apart in bigger grains, with no clear dependence on grain orientation and Schmid factor. Slip bands on secondary and tertiary slip planes develop similar spacings to those on primary planes, although the latter extend over larger regions of the grains. Once they occupy the entirety of a grain, the plastic strains within the slip bands keep increasing to accommodate the macroscopic deformation imposed.

The FFTD approach, with potential applications using other microscopy techniques, could enable much needed large scale quantitative studies of slip localisation for a variety of materials and loading conditions.

Competing interests

The authors declare none.

of hydrogen embrittlement, short range order, and second phase effects, among others.

Overall, the FFTD offers a number of unique advantages. The only other existing techniques capable of generating large scale quantitative analyses of slip band distribution are the Radon transform approach (Sperry et al., 2020) with slip system identification (Chen & Daly, 2017) and the Heaviside-DIC (Bourdin et al., 2018) with iterative Hough transformations (Charpagne et al., 2020, 2021), which can identify individual slip bands and their active slip systems. The approach by Chen and Daly (Chen & Daly, 2017) to determine the active slip system could also be incorporated to the current technique, albeit it needs to be automated. The FFTD approach in its current state, while not having access to the in-and-out of plane strain, fully preserves the geometry of the slip bands. This allows for the quantification of slip band widths and volume fractions (León-Cázares et al., 2020a). Another advantage of the FFTD is that it leverages the combined effect of multiple slip bands with a shared orientation to detect active slip planes. As such, it should be less likely to interpret cases of wavy slip as false positives (the only two instances being those in Figure 8 as they happened to be almost parallel lines) compared to other techniques. The FFTD could also be applied on images where the intensity corresponds to specific strain components (e.g. parallel to the slip band traces) to capture some of

References

Aboulfadl H, Deges J, Choi P & Raabe D (2015). Dynamic strain aging studied at the atomic scale, *Acta Mater.* **86**, 34–42, URL http://dx.doi.org/10.1016/j.actamat.2014.12.028https://linkinghub.elsevier.com/retrieve/pii/S1359645414009458.

Abu-Odeh A & Asta M (2022). Modeling the effect of short-range order on cross-slip in an FCC solid solution, *Acta Mater.* **226**, 117615, URL https://doi.org/10.1016/j.actamat.2021.117615https://linkinghub.elsevier.com/retrieve/pii/S1359645421009939.

Andani MT, Lakshmanan A, Karamooz-Ravari M, Sundararaghavan V, Allison J & Misra A (2020). A quantitative study of stress fields ahead of a slip band blocked by a grain boundary in unalloyed magnesium, *Sci. Rep.* **10**, 3084, URL http://www.nature.com/articles/s41598-020-59684-y.

Atkinson M, Thomas R, Harte A, Crowther P & Quinta da Fonseca J (2020). DefDAP, Deformation data analysis in Python, Zenodo.

Ayres CE, Jha BS, Meredith H, Bowman JR, Bowlin GL, Henderson SC & Simpson DG (2008). Measuring fiber alignment in electrospun scaffolds: a user's guide to the 2D fast Fourier transform approach, *J. Biomater. Sci., Polym. Ed.* **19**, 603–621, URL https://www.tandfonline.com/doi/full/10.1163/156856208784089643.

Bachmann F, Hielscher R & Schaeben H (2011). Grain detection from 2d and 3d EBSD data—Specification of the MTEX algorithm, *Ultramicroscopy* **111**, 1720–1733, URL http://dx.doi.org/10.1016/j.ultramic.2011.08.002https://linkinghub.elsevier.com/retrieve/pii/S0304399111001951.

Bali N (2008). *Golden Co-ordinate Geometry*, New Delhi: Laxmi Publications, 1 ed.

Birosca S (2015). The deformation behaviour of hard and soft grains in RR1000 nickel-based superalloy, *IOP Conf. Ser.: Mater. Sci. Eng.* **82**, 012033, URL https://iopscience.iop.org/article/10.1088/1757-899X/82/1/012033.

Bourdin F, Stinville J, Echlin M, Callahan P, Lenthe W, Torbet C, Texier D, Bridier F, Cormier J, Villechaise P, Pollock T & Valle V (2018). Measurements of plastic localization by heaviside-digital image correlation, *Acta Mater.* **157**, 307–325, URL https://doi.org/10.1016/j.actamat.2018.07.013https://linkinghub.elsevier.com/retrieve/pii/S135964541830541X.

Charpagne M, Hestroffer J, Polonsky A, Echlin M, Texier D, Valle V, Beyerlein I, Pollock T & Stinville J (2021). Slip localization in Inconel 718: A three-dimensional and statistical perspective, *Acta Mater.* **215**, 117037, URL https://doi.org/10.1016/j.actamat.2021.117037https://linkinghub.elsevier.com/retrieve/pii/S1359645421004171.

Charpagne M, Stinville J, Callahan P, Texier D, Chen Z, Villechaise P, Valle V & Pollock T (2020). Automated and quantitative analysis of plastic strain localization via multi-modal data recombination, *Mater. Charact.* **163**, 110245, URL https://doi.org/10.1016/j.matchar.2020.110245https://linkinghub.elsevier.com/retrieve/pii/S1044580319335569.

Chen Z & Daly SH (2017). Active Slip System Identification in Polycrystalline Metals by Digital Image Correlation (DIC), *Exp. Mech.* **57**, 115–127, URL http://link.springer.com/10.1007/s11340-016-0217-3.

Davis BL, Berrier JC, Shields DW, Kennefick J, Kennefick D, Seigar MS, Lacy CHS & Puerari I (2012). Measurement of galactic logarithmic spiral arm pitch angle using two-dimensional fast Fourier transform decomposition, *Astrophys. J., Suppl. Ser.* **199**, 33, URL https://iopscience.iop.org/article/10.1088/0067-0049/199/2/33.

Di Gioacchino F & Quinta da Fonseca J (2013). Plastic Strain Mapping with Sub-micron Resolution Using Digital Image Correlation, *Exp. Mech.* **53**, 743–754, URL http://link.springer.com/10.1007/s11340-012-9685-2.

Di Gioacchino F & Quinta da Fonseca J (2015). An experimental study of the polycrystalline plasticity of austenitic stainless steel, *Int. J. Plast.* **74**, 92–109, URL https://linkinghub.elsevier.com/retrieve/pii/S0749641915000820.

Edwards T, Di Gioacchino F, Springbett H, Oliver R & Clegg W (2017). Stable Speckle Patterns for Nano-scale Strain Mapping up to 700 °C, *Exp. Mech.* **57**, 1469–1482, URL http://link.springer.com/10.1007/s11340-017-0317-8.

Fallahi A & Ataee A (2010). Effects of crystal orientation on stress distribution near the triple junction in a tricrystal γ-TiAl, *Mater. Sci. Eng. A* **527**, 4576–4581, URL https://linkinghub.elsevier.com/retrieve/pii/S092150931000314X.

Gaskey B, Hendl L, Wang X & Seita M (2020). Optical characterization of grain orientation in crystalline materials, *Acta Mater.* **194**, 558–564, URL https://linkinghub.elsevier.com/retrieve/pii/S1359645420303748.

Gibson JSKL, Pei R, Heller M, Medghalchi S, Luo W & Korte-Kerzel S (2021). Finding and Characterising Active Slip Systems: A Short Review and Tutorial with Automation Tools, *Materials* **14**, 407, URL https://www.mdpi.com/1996-1944/14/2/407.

Guo Y, Britton T & Wilkinson A (2014). Slip band–grain boundary interactions in commercial-purity titanium, *Acta Mater.* **76**, 1–12, URL http://dx.doi.org/10.1016/j.actamat.2014.05.015https://linkinghub.elsevier.com/retrieve/pii/S1359645414003632.

Harte A, Atkinson M, Preuss M & Quinta da Fonseca J (2020). A statistical study of the relationship between plastic strain and lattice misorientation on the surface of a deformed Ni-based superalloy, *Acta Mater.* **195**, 555–570, URL https://doi.org/10.1016/j.actamat.2020.05.029https://linkinghub.elsevier.com/retrieve/pii/S1359645420303761.

He F, Wei S, Cann JL, Wang Z, Wang J & Tasan CC (2021). Composition-dependent slip planarity in mechanically-stable face centered cubic complex concentrated alloys and its mechanical effects, *Acta Mater.* **220**, 117314, URL https://doi.org/10.1016/j.actamat.2021.117314https://linkinghub.elsevier.com/retrieve/pii/S1359645421006947.

Hielscher R & Schaeben H (2008). A novel pole figure inversion method: specification of the MTEX algorithm, *J. Appl. Crystallogr.* **41**, 1024–1037, URL http://scripts.iucr.org/cgi-bin/paper?S0021889808030112.

Ho H, Risbet M & Feaugas X (2015). On the unified view of the contribution of plastic strain to cyclic crack initiation: Impact of the progressive transformation of shear bands to persistent slip bands, *Acta Mater.* **85**, 155–167, URL https://linkinghub. elsevier.com/retrieve/pii/S1359645414008647.

Hormann K & Agathos A (2001). The point in polygon problem for arbitrary polygons, *Comput. Geom.* **20**, 131–144, URL https://linkinghub.elsevier.com/retrieve/pii/ S0925772101000128.

Jiang J, Dunne FPE & Britton TB (2017). Toward Predictive Understanding of Fatigue Crack Nucleation in Ni-Based Superalloys, *JOM* **69**, 863–871, URL http://link.springer.com/ 10.1007/s11837-017-2307-9.

Kim JM, Kim SJ & Kang JH (2022). Effects of short-range ordering and stacking fault energy on tensile behavior of nitrogen-containing austenitic stainless steels, *Mater. Sci. Eng. A* **836**, 142730, URL https://doi.org/10.1016/j.msea.2022.142730https: //linkinghub.elsevier.com/retrieve/pii/S0921509322001381.

Kim SD, Park JY, Park SJ, hoon Jang J, Moon J, Ha HY, Lee CH, Kang JY, Shin JH & Lee TH (2019). Direct observation of dislocation plasticity in high-Mn lightweight steel by in-situ TEM, *Sci. Rep.* **9**, 15171, URL http://www.nature.com/articles/ s41598-019-51586-y.

Koehler JS (1952). The Nat. of Work-Hardening, *Phys. Rev.* **86**, 52–59, URL https://link.aps.org/doi/10.1103/PhysRev.86.52.

Kundu A, Field DP & Chandra Chakraborti P (2019). Influence of strain amplitude on the development of dislocation structure during cyclic plastic deformation of 304 LN austenitic stainless steel, *Mater. Sci. Eng. A* **762**, 138090, URL https://doi.org/10.1016/j.msea.2019.138090https: //linkinghub.elsevier.com/retrieve/pii/S0921509319308767.

Lavenstein S, Gu Y, Madisetti D & El-Awady JA (2020). The heterogeneity of persistent slip band nucleation and evolution in metals at the micrometer scale, *Science* **370**, eabb2690, URL https://www.sciencemag.org/lookup/doi/10.1126/science. abb2690.

León-Cázares F, Monni F, Jackson T, Galindo-Nava E & Rae C (2020a). Stress response and microstructural evolution of nickel-based superalloys during low cycle fatigue: Physics-based modelling of cyclic hardening and softening, *Int. J. Plast.* **128**, 102682, URL https://doi.org/10.1016/j.ijplas.2020.102682https: //linkinghub.elsevier.com/retrieve/pii/S0749641919307247.

León-Cázares F, Schlütter R, Jackson T, Galindo-Nava E & Rae C (2020b). A multiscale study on the morphology and evolution of slip bands in a nickel-based superalloy during low cycle fatigue, *Acta Mater.* **182**, 47–59, URL https://linkinghub. elsevier.com/retrieve/pii/S1359645419306950.

León-Cázares FD & Rae CMF (2020). A Stress Orientation Analysis Framework for Dislocation Glide in Face-Centred Cubic Metals, *Crystals* **10**, 445, URL https://www.mdpi.com/ 2073-4352/10/6/445.

Lerch BA & Gerold V (1987). Cyclic hardening mechanisms in NIMONIC 80A, *Metall. Trans. A* **18**, 2135–2141, URL http: //link.springer.com/10.1007/BF02647085.

Lerch BA, Jayaraman N & Antolovich SD (1984). A study of fatigue damage mechanisms in Waspaloy from 25 to 800°C, *Mater. Sci. Eng.* **66**, 151–166, URL https://linkinghub.elsevier. com/retrieve/pii/0025541684901770.

Li X, Li C, Lu L, Huang J & Luo S (2021). Interactions between slip bands and interfaces in a compressed duplex stainless steel, *Mater. Sci. Eng. A* **818**, 141325, URL https://linkinghub. elsevier.com/retrieve/pii/S0921509321005943.

Lukáš P & Kunz L (2004). Role of persistent slip bands in fatigue, *Philos. Mag.* **84**, 317–330, URL http://www. tandfonline.com/doi/abs/10.1080/14784430310001610339.

Lunt D, Busolo T, Xu X, Quinta da Fonseca J & Preuss M (2017). Effect of nanoscale α 2 precipitation on strain localisation in a two-phase Ti-alloy, *Acta Mater.* **129**, 72–82, URL https://linkinghub.elsevier.com/retrieve/pii/ S1359645417301696.

Malek AS, Drean JY, Bigue L & Osselin JF (2013). Optimization of automated online fabric inspection by fast Fourier transform (FFT) and cross-correlation, *Text. Res. J.* **83**, 256–268, URL http://journals.sagepub.com/doi/10.1177/ 0040517512458340.

Mangal A & Holm EA (2018). Applied machine learning to predict stress hotspots I: Face centered cubic materials, *Int. J. Plast.* **111**, 122–134, URL https://doi.org/10.1016/j.ijplas.2018.07.013https: //linkinghub.elsevier.com/retrieve/pii/S0749641918302365.

Ménard M, Olive J, Brass AM & Aubert I (2008). Effects of hydrogen charging on surface slip band morphology of a type 316L stainless steel, *Environ.-Induced Cracking Mater.*, 179–188, Elsevier, URL https://linkinghub.elsevier.com/retrieve/pii/ B9780080446356500170.

Mughrabi H (2009). Cyclic Slip Irreversibilities and the Evolution of Fatigue Damage, *Metall. Mater. Trans. B* **40**, 431–453, URL http://link.springer.com/10.1007/s11663-009-9240-4.

Mughrabi H (2013). Microstructural fatigue mechanisms: Cyclic slip irreversibility, crack initiation, non-linear elastic damage analysis, *Int. J. Fatigue* **57**, 2–8, URL http://dx.doi.org/10.1016/j.ijfatigue.2012.06.007https: //linkinghub.elsevier.com/retrieve/pii/S0142112312002083.

Nibur KA, Bahr DF & Somerday BP (2006). Hydrogen effects on dislocation activity in austenitic stainless steel, *Acta Mater.* **54**, 2677–2684, URL https://linkinghub.elsevier.com/retrieve/ pii/S1359645406001327.

Ospina-Correa JD, Olaya-Muñoz DA, Toro-Castrillón JJ, Toro A, Ramírez-Hernández A & Hernández-Ortíz JP (2021). Grain polydispersity and coherent crystal reorientations are features to foster stress hotspots in polycrystalline alloys under load, *Sci. Adv.* **7**, 1–10, URL https://www.science.org/doi/ 10.1126/sciadv.abe3890.

Petrenec M, Polák J, Samoril T, Dluhos J & Obrtlík K (2014). In-Situ High Temperature Low Cycle Fatigue Study of Surface Topography Evolution in Nickel Superalloys, *METAL 2014 Int. Conf. Metal. Mater.,23rd*, 1139–1144, Brno.

Polák J & Man J (2014). Mechanisms of extrusion and intrusion formation in fatigued crystalline

materials, *Mater. Sci. Eng. A* **596**, 15–24, URL http://dx.doi.org/10.1016/j.msea.2013.12.005https://linkinghub.elsevier.com/retrieve/pii/S0921509313013543.

Ram F, Zaefferer S & Raabe D (2014). Kikuchi bandlet method for the accurate deconvolution and localization of Kikuchi bands in Kikuchi diffraction patterns, *J. Appl. Crystallogr.* **47**, 264–275, URL https://scripts.iucr.org/cgi-bin/paper?S1600576713030446.

Risbet M & Feaugas X (2008). Some comments about fatigue crack initiation in relation to cyclic slip irreversibility, *Eng. Fract. Mech.* **75**, 3511–3519, URL https://linkinghub.elsevier.com/retrieve/pii/S001379440700224X.

Risbet M, Feaugas X, Guillemer-Neel C & Clavel M (2003). Use of atomic force microscopy to quantify slip irreversibility in a nickel-base superalloy, *Scr. Mater.* **49**, 533–538.

Sangid MD (2013). The physics of fatigue crack initiation, *Int. J. Fatigue* **57**, 58–72, URL http://dx.doi.org/10.1016/j.ijfatigue.2012.10.009.

Sangid MD, Rotella J, Naragani D, Park JS, Kenesei P & Shade PA (2020). A complete grain-level assessment of the stress-strain evolution and associated deformation response in polycrystalline alloys, *Acta Mater.* **201**, 36–54, URL https://linkinghub.elsevier.com/retrieve/pii/S135964542030745X.

Sperry R, Han S, Chen Z, Daly SH, Crimp MA & Fullwood DT (2021). Comparison of EBSD, DIC, AFM, and ECCI for active slip system identification in deformed Ti-7Al, *Mater. Charact.* **173**, 110941, URL https://doi.org/10.1016/j.matchar.2021.110941https://linkinghub.elsevier.com/retrieve/pii/S1044580321000711.

Sperry R, Harte A, Quinta da Fonseca J, Homer ER, Wagoner RH & Fullwood DT (2020). Slip band characteristics in the presence of grain boundaries in nickel-based superalloy, *Acta Mater.* **193**, 229–238, URL https://linkinghub.elsevier.com/retrieve/pii/S1359645420303025.

Stinville J, Callahan P, Charpagne M, Echlin M, Valle V & Pollock T (2020). Direct measurements of slip irreversibility in a nickel-based superalloy using high resolution digital image correlation, *Acta Mater.* **186**, 172–189, URL https://linkinghub.elsevier.com/retrieve/pii/S1359645419308389.

Stinville J, Vanderesse N, Bridier F, Bocher P & Pollock T (2015). High resolution mapping of strain localization near twin boundaries in a nickel-based superalloy, *Acta Mater.* **98**, 29–42, URL http://dx.doi.org/10.1016/j.actamat.2015.07.016https://linkinghub.elsevier.com/retrieve/pii/S1359645415004784.

Stinville JC, Charpagne MA, Cervellon A, Hemery S, Wang F, Callahan PG, Valle V & Pollock TM (2022). On the origins of fatigue strength in crystalline metallic materials, *Science* **377**, 1065–1071, URL https://www.science.org/doi/10.1126/science.abn0392.

Valsan M, Sastry DH, sankara Rao KB & Mannan SL (1994). Effect of strain rate on the high-temperature low-cycle fatigue properties of a nimonic PE-16 superalloy, *Metall. Mater. Trans. A* **25**, 159–171, URL http://link.springer.com/10.1007/BF02646684.

Yu H, Cocks A & Tarleton E (2019). Discrete dislocation plasticity HELPs understand hydrogen effects in bcc materials, *J. Mech. Phys. Solids* **123**, 41–60, URL https://doi.org/10.1016/j.jmps.2018.08.020https://linkinghub.elsevier.com/retrieve/pii/S002250961830574X.